



NRL/MR/5673--98-8310

Analysis of Pendulated Load Response and T-ACS/Lighter Interaction in a 1:24 Scale Model JLOTS Cargo Transfer Operation at the David Taylor Model Basin in 1997

MICHAEL TODD
SANDEEP VOHRA
CHRIS VANDETTE
JONATHAN NICHOLS

*Optical Techniques Branch
Optical Sciences Division*

October 30, 1998

19981103 094

Approved for public release; distribution unlimited.

REPORT DOCUMENTATION PAGE			Form Approved OMB No. 0704-0188	
Public reporting burden for this collection of information is estimated to average 1 hour per response, including the time for reviewing instructions, searching existing data sources, gathering and maintaining the data needed, and completing and reviewing the collection of information. Send comments regarding this burden estimate or any other aspect of this collection of information, including suggestions for reducing this burden, to Washington Headquarters Services, Directorate for Information Operations and Reports, 1215 Jefferson Davis Highway, Suite 1204, Arlington, VA 22202-4302, and to the Office of Management and Budget, Paperwork Reduction Project (0704-0188), Washington, DC 20503.				
1. AGENCY USE ONLY (Leave Blank)	2. REPORT DATE October 30, 1998	3. REPORT TYPE AND DATES COVERED NRL Memorandum Report		
4. TITLE AND SUBTITLE Analysis of Pendulated Load Response and T-ACS/Lighter Interaction in a 1:24 Scale Model JLOTS Cargo Transfer Operation at the David Taylor Model Basin in 1997			5. FUNDING NUMBERS	
6. AUTHOR(S) Michael Todd, Sandeep Vohra, Chris Vandette, and Jonathan Nichols				
7. PERFORMING ORGANIZATION NAME(S) AND ADDRESS(ES) Naval Research Laboratory Washington, DC 20375-5320			8. PERFORMING ORGANIZATION REPORT NUMBER NRL/PU/5610-98-357 NRL/MR/5673-98-8310	
9. SPONSORING/MONITORING AGENCY NAME(S) AND ADDRESS(ES) Naval Surface Warfare Center			10. SPONSORING/MONITORING AGENCY REPORT NUMBER	
11. SUPPLEMENTARY NOTES				
12a. DISTRIBUTION/AVAILABILITY STATEMENT Approved for public release; distribution unlimited.			12b. DISTRIBUTION CODE	
13. ABSTRACT (Maximum 200 words) A 1:24 scale model test of a Joint-Logistics-Over-The-Shore (JLOTS) at-sea cargo transfer operation was conducted at the David Taylor Model Basin (NSWC-Carderock) in July and August of 1997. The test specifically consisted of a container ship, T-ACS ¹ class crane ship with motorized model crane, and lighterage, all subject to various sea states, crane configurations, ship headings, implementation of rider block/tag line (RBTS) control, and load types (20 foot container and VLS missile cannister). Forty-six channels of information were gathered for each run, which typically lasted about 8 minutes. For certain conditions, <i>load pendulation</i> is reported, and an analysis of the nonlinear aspects of these oscillations yields dual-time scale behavior, which may be chaotic in certain conditions. In addition, impacts between T-ACS and lighter barges were noted during the tests, and a preliminary analysis of this phenomenon is included.				
14. SUBJECT TERMS			15. NUMBER OF PAGES 36	
			16. PRICE CODE	
17. SECURITY CLASSIFICATION OF REPORT UNCLASSIFIED	18. SECURITY CLASSIFICATION OF THIS PAGE UNCLASSIFIED	19. SECURITY CLASSIFICATION OF ABSTRACT UNCLASSIFIED	20. LIMITATION OF ABSTRACT UL	

Contents

1	JLOTS Operations and The Load Pendulation Problem	1
2	The 1:24 Scale Model Test	3
3	Occurrence of Pendulation	6
4	Dynamics of Crane Load Time Series	11
1	Modeling and The Spherical Pendulum	11
2	The Chaotic Nature of the Pendulation Oscillations	13
3	Application to Model Test Crane Load Oscillations	18
5	T-ACS/Lighter Impact Events	19
6	Summary and Conclusions	22
7	Acknowledgments	23
A	Appendix: Channel Summary for 1:24 Scale Model Test	26
B	Appendix: Flexural Disc Dynamics Theory	27
C	Appendix: Mathematical Modeling of the Spherical Pendulum	29

ANALYSIS OF PENDULATED LOAD RESPONSE AND T-ACS/LIGHTER INTERACTION IN A 1:24 SCALE MODEL JLOTS CARGO TRANSFER OPERATION AT THE DAVID TAYLOR MODEL BASIN 1997

1. JLOTS Operations and The Load Pendulation Problem

An increasingly important role of the U.S. Navy surface fleet is its ability to respond quickly and efficiently to a local or regional crisis. The Defense Planning Guidance for fiscal years 1994-1999 stipulated that the Navy must “maintain a broad range of capabilities, particularly emphasizing enhanced mobility to enable [the deployment of] sizable forces over long distances on short notice” [1]. One of the primary elements in maintaining this ability is the efficiency of logistics operations, and, more specifically, Joint Logistics Over The Shore (JLOTS) operations. JLOTS operations are defined as logistics operations—typically the unloading of ships without the benefit of fixed port facilities—conducted by two or more military branch forces under a single commander. During phases of theater development in wartime or in either friendly or undefended territory, plans for JLOTS operations rely upon strategic sealifting of containerized cargo, *e.g.*, up to 95% of dry cargo such as military hardware and up to 99% of petroleum products, to the points of operation. As the ships available for these sealifting duties shifted to large bulk containerships, heavy-lift barges, and deep-draft tankers, the need arose for the downloading of these vessels while they remained anchored offshore. By the 1970s, the military had developed a number of subsystems designed to achieve this task, and one such subsystem was the T-ACS auxiliary crane ship, whose function was to download container ship cargo on to ship-to-shore lighterage, as shown in Figure 1. These crane ships utilize operator-controlled cranes to lift, move, and discharge the cargo between subsystems. During at-sea JLOTS exercises in 1991-1993, the appearance of storm fronts demonstrated an inherent problem associated with this specific operation. As the sea state increased from 2 to 3 (as defined by the Pierson-Moskowitz Sea Spectrum, with significant wave heights in the 3.5 ft to 5.0 ft range), transfer operations had to be ceased due to *load pendulation* of the cargo while being moved by the cranes. Large-scale, complex motions of the load were observed, rendering its safe control difficult (at least within the current seamanship ability of crane operators due to lack of experience), thus leading to diminished productive transfer time and degraded throughput capability. Even relatively small crane ship motions, *e.g.*, a 1° hull roll, have been known to induce dangerous load pendulation. Time histories of coastal sea conditions worldwide have indicated that sea state 3 conditions occur on average about 20% of the time, and conditions higher than sea state 3 occur on average about 15% of the time [1]. Given the

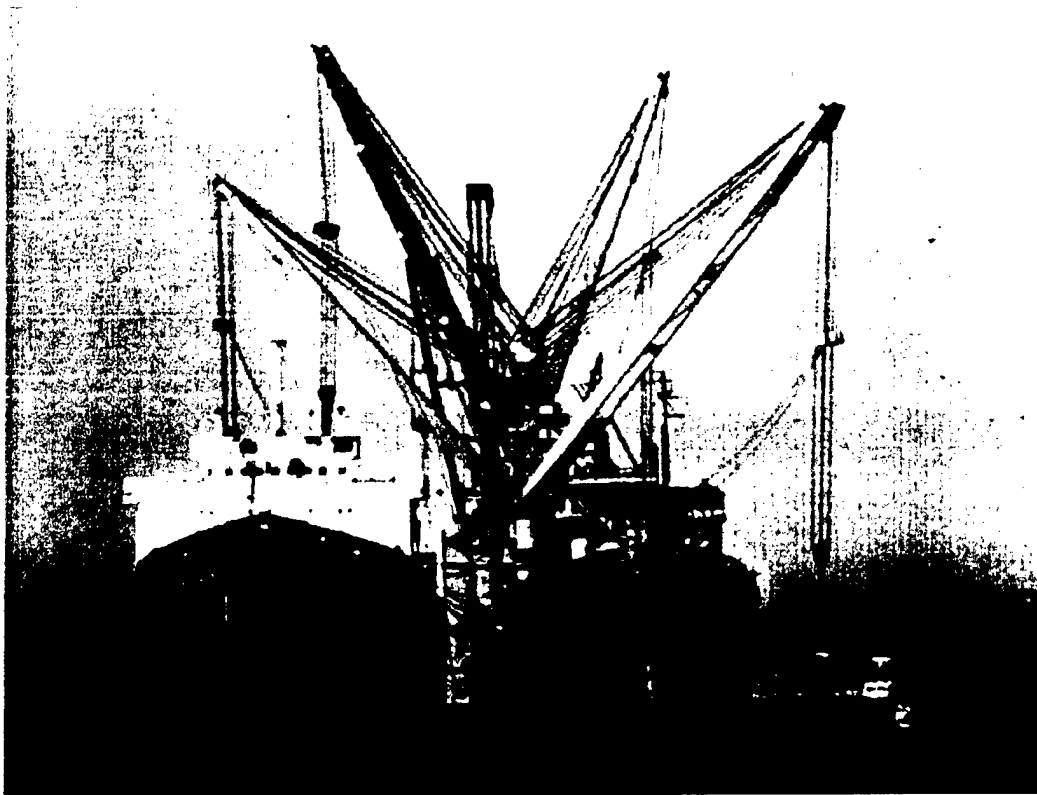


Figure 1. A typical JLOTS scenario involving the downloading of container ship cargo to ship-to-shore lighterage.

dangerous nature of operating the current subsystems in these higher sea states, interest arose in understanding the pendulation problem at a fundamental dynamics level: what is the nature of the complex motion and where does it occur? Specific interest has been aimed at determining whether the motion might be *chaotic*² or not, with the implication that chaotic dynamics may lead to different advanced control strategies [2].

This report will first discuss the scaled model test, including a description of the fiber optic accelerometer array system designed and optical radar used to interrogate the lighter barges and the load, respectively. Load motions from the test will then be analyzed for the *nonlinear* aspects of their dynamic character and will be compared to spherical pendulum models developed to explain the nature of the dynamics. Important results from the mathematical model analysis (including comparison to a spherical pendulum experiment on a Stewart platform forcing table in the laboratory) regarding the occurrence of

² The notion of chaotic behavior will be examined later in this report.

resonant dynamics—leading to probable chaotic oscillations—will be summarized. Under certain conditions, it will be shown that the load motions are likely chaotic, due to a positive Lyapunov exponent spectrum³. Summaries regarding under which sea and crane configurations pendulation was observed will be presented. Finally, a summary of T-ACS crane ship-to-lighter impact events will be given.

2. The 1:24 Scale Model Test

The 1:24 scale model JLOTS test was conducted in the seakeeping basin of the David Taylor Model Basin at Naval Surface Warfare Center (NSWC)-Carderock (Carderock, MD) during July and August, 1997. All ship models were designed and built at NSWC, and two crane models were built, one by the University of Colorado-Denver and one by USA Models Inc. The cranes were designed to retain most of the motorized features that the full-scale cranes have, including luff and slew control of the boom, load hoist capability, and a rider block/tag line (RBTS) load control system. The single unscaled feature was the motor power, which was significantly greater at the model scale.

The test itself consisted of 251 different trials, each running approximately 8 minutes long, under a matrix of variable conditions, including sea state (3, 3+swell, 4, 4+swell), ship heading relative to incoming waves (in 45° increments between 0° and 360°), ship configuration⁴, crane configuration (various slew and luff angles), RBTS implementation (with and without rider block and at various tag line tensions), and load type (20 foot container and VLS missile cannister). Forty-six channels of data were recorded, including T-ACS and containership bulk motions (*i.e.*, roll, pitch, heave, *etc.*), lighter motions, relative ship motions, load motion, and significant wave height (related to sea state); a summary of the measurands is given in Table 2 in Appendix A. A typical test configuration is shown in Figure 2.

An array of 14 fiber optic (FO) accelerometers were designed to detect motions of the lighter train. Such structural-grade sensing requires high acceleration sensitivity, a flat

³ The concept of a Lyapunov exponent will be discussed briefly later in this report.

⁴ The most common configuration was the T-ACS ship in the center with the container ship to starboard and the lighter to port, and the secondary configuration was the T-ACS ship with container ship removed and the DD-963 to starboard.

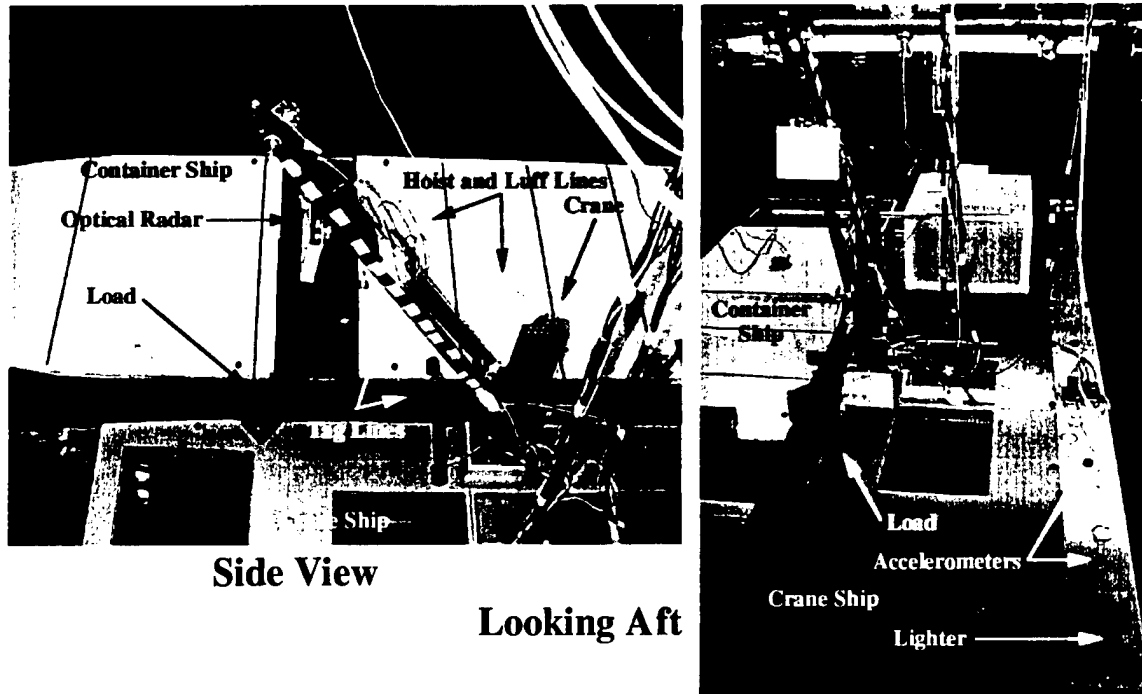


Figure 2. The 1:24 scale model JLOTS test.

low-frequency operational band (between about 0.3 Hz and 20 Hz), low cross-axis sensitivity, immunity from extraneous measurands, and small size and weight. The most common approach for designing such FO accelerometers involve coupling the acceleration-induced motions of a flexural disc (subject to some boundary conditions) to a coil of optical fiber, which is made part of a FO interferometer. The disc, the fiber, and the interferometer are placed inside a protective housing, and tailoring the geometry of the disc and the interferometer characteristics determine the performance of the sensor; specifically, the flexural disc dimensions and total fiber length determine the intrinsic scale factor or sensitivity of the accelerometer, while the inherent physical characteristics of the disc and its boundary conditions determine the resonant frequency [3]. Appendix B provides a discussion on flexural disc dynamics that serves as the underlying theory behind the design.

The specific design chosen for this model test was a center-supported, circular aluminum disc (33 mm diameter, 0.25 mm thick), as shown in Figure 3. A 3-gram circumferential ring weight was bonded around the edge of the disc to enhance its response to acceleration excitation. The phase shift in the interferometer was recovered using a phase-generated carrier scheme [4], where the electronics used in sensor interrogation were tuned to roll

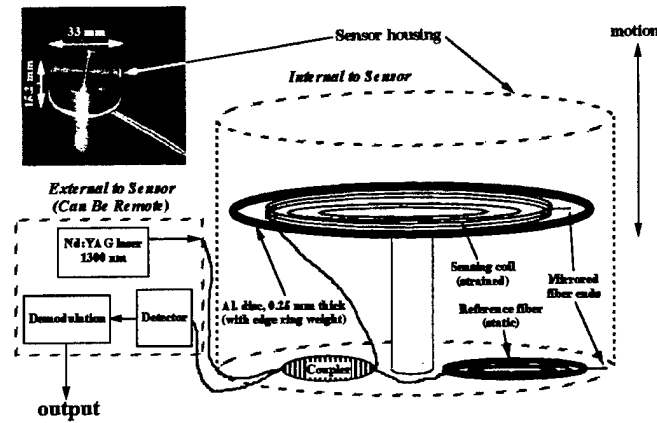


Figure 3. A schematic of the FO sensors system used in the test.

Characteristic	Value
Size	33 mm dia., 0.25 mm thick
Mass	<60 grams
Axial responsivity	>40 dB re rad/g
Cross-axis sensitivity	<30 dB down from axial
Pressure sensitivity	<190 dB rad/ μ Pa

Table 1. Performance characteristics for a typical sensor from the array.

off near 0.2 Hz. With a total fiber length of 10.1 meters, these specifications resulted in a sensitivity of approximately 40 dB radians/g, a resonant frequency near 1 kHz, and a minimum detectable acceleration of about -75 dB $g/\sqrt{\text{Hz}}$ at 0.3 Hz. The minimum limit was determined by placing the sensor in an acoustically-isolated, lead-lined foam box; the phase noise limit is also shown in the figure. Improved isolation of the sensor from the environment would result in the minimum detection limit approaching the phase noise limit. The frequency response and minimum detection limit for a typical one of these sensors are shown in Figure 4. These and other performance characteristics are summarized in Table 1. A more complete system description can be found in [5].

Because of the problems associated with using accelerometry in systems subject to gravitational restoring forces (*i.e.*, free-fall conditions), such as the crane load, the fiber optic accelerometer system could not be utilized for load motion detection. An optical

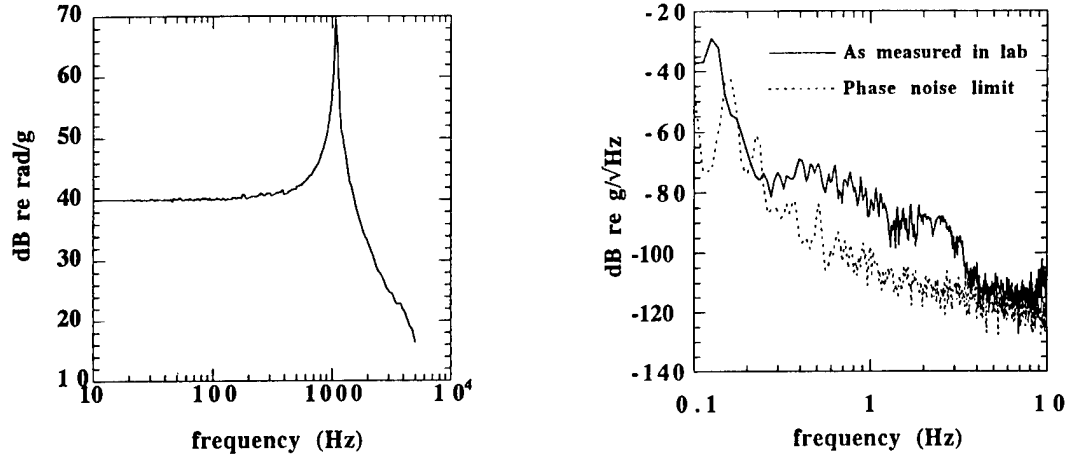


Figure 4. The frequency response (left) and minimum detection limit (right) of a typical FO accelerometer from the array.

radar (called the DynasightTM), produced by Origin Instruments of Grand Prairie, TX, was used to track, in real time, a small active, modulated, infrared LED target that had been mounted on the crane load. Feedback from the LED was fed into the DynasightTM to induce frequency locking upon the LED signal, and on-board time-of-flight algorithms then returned the displacement of the LED in all three Cartesian dimensions, relative to a fixed point on the DynasightTM. The digital data output from the sensor, updated at 64 Hz and sent in standard RS-232 serial format, were sent to a serial port on a PC, where decompensating and scaling were done in the LabVIEWTM virtual instrument environment⁵. It was found that the raw output from the DynasightTM required no digital filtering or other signal processing. If the LED mounted on the load traveled outside the vision cone of the DynasightTM, the last known position was stored in memory until the LED target was reacquired. Any periods of lost target lock⁶ would result in flat lines in the displacement trace output from the radar, which could be monitored for loss of robustness in a given data set. The sensor nominally has a resolution of about 0.05 mm per least significant bit (with 32-bit data), but a base-2 exponent field is carried with the displacement data to allow for a variable sensitivity; such an approach allows for the proper scaling that gives a wide dynamic range while maintaining good measurement resolution.

⁵ LabVIEWTM is a registered trademark of National Instruments Inc, Austin, TX.

⁶ Loss of target lock would result from large excursions of the load LED, usually during a pendulation event.

3. Occurrence of Pendulation

Various combinations of sea states, crane configuration, and RBTS implementation can induce large-scale load oscillations (pendulation)⁷. The prevailing sea state, with energy over some frequency band, causes the T-ACS to respond in turn, usually dominated by its natural roll frequency. The ship's motion subsequently induces motion of the crane structure affixed to it, and finally, that resulting motion induces oscillations of the load (Figure 5). The response of the load is influenced primarily by the proximity of excitation to its own resonance. Pendulum-like systems such as a crane load suspended from a boom have a resonant frequency defined by

$$f_{res} = \frac{1}{2\pi} \sqrt{\frac{g}{L}}, \quad (1)$$

where g is the gravitational constant and L is the distance from the point of suspension to the center of mass of the load.

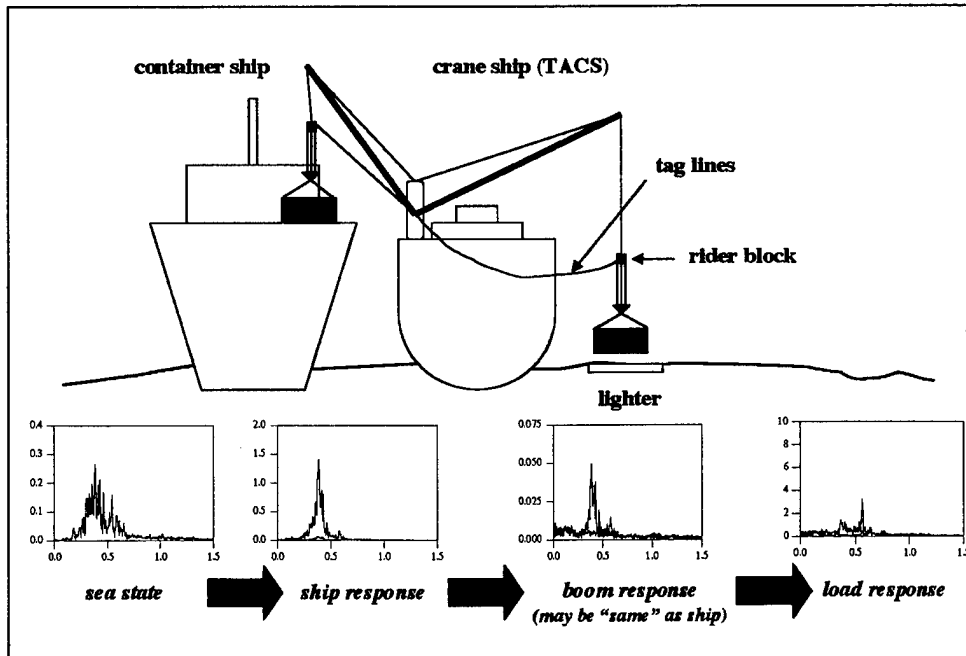


Figure 5. Pendulation occurs under certain combinations of sea state, ship response, and crane response.

⁷ The remainder of this report will focus on the first 182 runs conducted in the test; a future report will address the remaining runs.

If no RBTS is present, or the tag lines are completely slack, the length L is simply the distance from the boom tip to the load mass center⁸. Longer distances L (such as when the luff angle is large, and the load is dropped very low during deposition upon the lighter) lead to a reduction of the resonant frequency such that it falls well within the sea state band. The use of the RBTS effectively serves to anchor the load at a different point such that the effective pendulation length is decreased. The rider block can be raised or lowered along the hoist line to the desired height, and then the tag lines are drawn inward to provide tension at that location. This latter tag line action is important, as the rider block itself provides relatively little mass (compared to the load) with which to alter the pendulation length, *i.e.*, resonance, by itself. If the tag lines are left completely slack, pendulation will typically still occur as if no RBTS were present. A potentially worse scenario may occur when the tag lines are pulled in partially such that the load senses their presence only during one part of its oscillation; this situation introduces a strong discontinuity into the load's restoring force, which has been shown by a number of authors to promote complex nonlinear dynamics [6, 7, 8, 9].

These pendulation events can be broadly classified into three categories: 1-D pendulation (pendulation in only one coordinate direction), 2-D pendulation (pendulation in both coordinate directions, or the plane), or no pendulation. These types of motion are typified in Figure 6. Pendulated motions in this model scale were roughly defined to be a 1.5 inch-amplitude root mean square value. When compared on the same scale, the magnitude of the various oscillations in Figure 6 becomes apparent: pendulating oscillations are significantly larger than non-pendulating ones, and no "intermediate" ground was achieved. The danger of these oscillations is self-evident, as 15 inch swings in the model scale correspond to 30 foot swings in the full scale. Also shown in Figure 6 are projections of both coordinate plane oscillations in each case to give a view to the spatial nature of the motion. In non-pendulation runs, the load (compared to other cases) remains relatively stationary, a point in the plane (Figure 6(a)). In the 1-D pendulation case, the motion is primarily confined to a region along the y-axis (Figure 6(b)), and in the 2-D case, motion fills both directions in the plane (Figure 6(c)). A more thorough discussion of these motions will occur later in this report. Figure 7 summarizes the occurrences of pendulating oscillations for sea states

⁸ It is being implicitly assumed that the hoist cabling is "rigid" in some sense. It should be noted that the cable has its own dynamics (due to its elasticity), but this has a secondary effect upon the nature of pendulation.

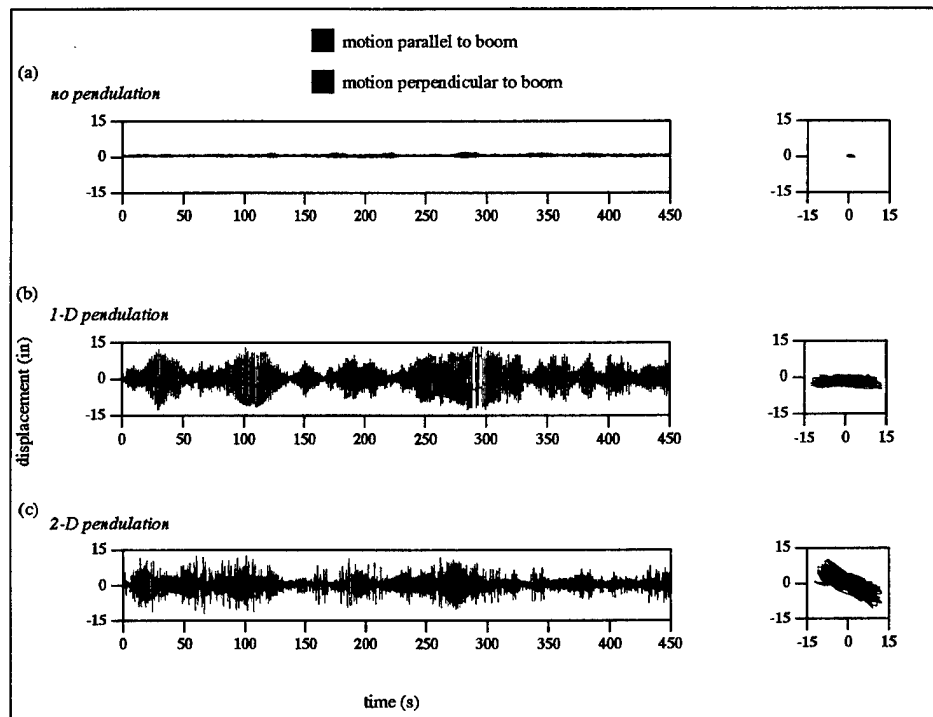


Figure 6. Classifications of pendulation events in the load response.

3 and 4 (with and without swell components, indicated by a "+" sign) in different ship headings⁹ and various RBTS and crane configurations. The T-ACS crane ship is much stiffer in pitch than in roll, and roll motions were typically much larger than pitch motions; as a result, excitation of the roll motion (such as with beam seas) coupled with the proper crane slew angle can result in violent pendulation. A slew angle of 0° means the boom is aligned with the long axis of the T-ACS. Pendulated motions are described by asterisks, with red asterisks indicating pendulated motion perpendicular to the boom and blue asterisks indicating pendulated motion parallel to the boom; thus, a single asterisk means 1-D pendulation, and two asterisks mean 2-D pendulation. In a number of cases, the run had to be stopped quickly due to severe pendulation¹⁰, and data were not officially recorded, although pendulation was observed visually. These cases are labeled "severe pendulation" in the table.

Regardless of sea state or crane configuration, the absence of RBTS ("no block") led to pendulation in all cases, as resonance was strongly excited due to the length L corresponding

⁹ Head seas indicate wave propagation along the long axis of the ship, beam seas indicate propagation along the short axis, and bow seas indicate propagation at 45° to the ship bow.

¹⁰ These cases sometimes led to snapped or tangled hoist/tag lines, a broken rider block, and other equipment damage.

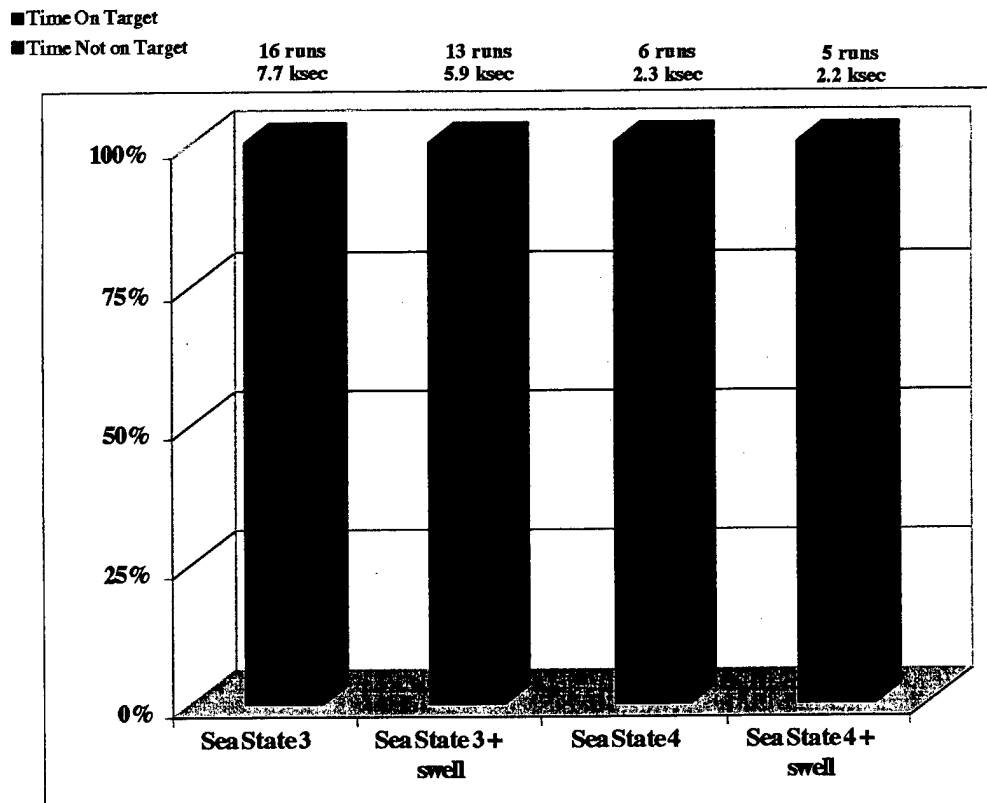


Figure 8. The percentages of time that the optical radar spent out of target lock .

total time spent in sea states 3, 3+, and 4+, less than 8% of the time was spent out of lock in each case; at sea state 4, almost 20% of the time was spent out of lock. In this latter case, detailed data analysis cannot be done without careful consideration of the loss-of-lock events.

4. Dynamics of Crane Load Time Series

4.1 Modeling and The Spherical Pendulum

The bottom left corner of Figure 9 shows one (pendulating) crane load time series example from the test. If a shorter segment of the time series is viewed (as at the top of the figure), two distinct scales of oscillatory behavior are observed. There is a strong “fast” oscillation (on the order of 1 Hz) on top of which much slower amplitude modulations are occurring

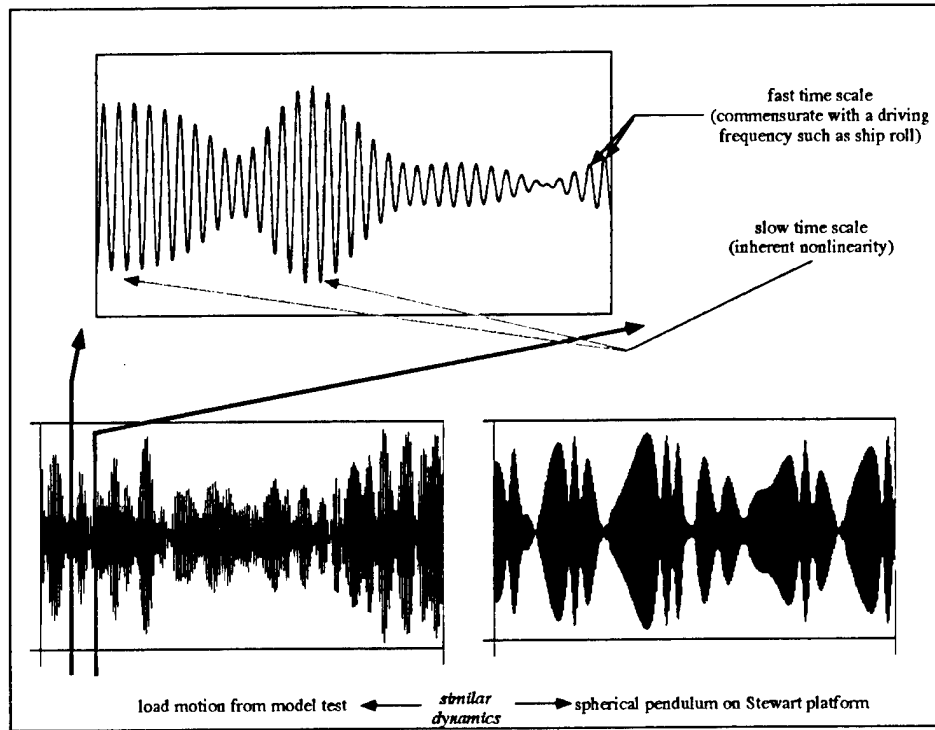


Figure 9. The load response oscillates at two distinct time scales—a slow amplitude modulation of a fast oscillation.

(on the order of 0.01 Hz). Such a dynamical phenomenon is called “two-timing” and is a common feature of weakly nonlinear systems [10].

Another mechanical system that captures this same two-timing feature, yet is somewhat more simple allowing for detailed study and mathematical modeling, is the forced *spherical pendulum*, as studied in [11, 12, 13]. The spherical pendulum is suspended from a universal joint so that it can oscillate in two planar directions, much like the crane load. The time series of the pendulum appear very similar to those of the crane load, as seen by comparing the bottom figures of Figure 9. The pendulum (and the crane load) oscillate back-and-forth at the fast frequency while the axis of that oscillation wanders around circumferentially at the slow frequency, even changing directions. The previously mentioned studies have shown that when the pendulum is excited in a band near its resonance (again determined by Equation (1)), these amplitude modulations appear, causing large-scale oscillations that can go out-of-plane, *even when the input excitation (ship motion) is completely tonal and in-plane*. Mathematically, this behavior can be explained by the onset of a supercritical Hopf bifurcation [14], where stationarity in the slow time scale spontaneously gives rise

to oscillations (manifest as amplitude modulations), while the fast-time oscillations remain unaffected.

A detailed experimental and theoretical study of this transition through resonance can be found in [15] and [16], and a summary will be now included in this report. If the pendulum is excited far away from resonance, the resulting motion is primarily *linear*, with damping-induced transient decay on to a steady, unmodulated motion oscillating at the primary driving frequency¹¹. As resonance is approached from frequencies above, a series of amplitude-modulations begin, which are first regular and periodic but eventually become complex (Figure 10)¹². These complex oscillations are not of a transient nature and have been observed to sustain themselves for at least one hour in the laboratory. It is of practical interest to know under what conditions these oscillations occurred. Under variations of forcing amplitude (corresponding to ship rolling or pitching amplitude) and forcing frequency (corresponding to ship rolling or pitching frequency), the various regions of qualitatively different dynamical behavior were charted out, as in Figure 11. There is a “V”-shaped region emanating from resonance (0.861 Hz for this particular pendulum) where modulated waveforms are observed; as the forcing amplitude is increased from near zero, these modulated motions are seen over an increasingly wide frequency band. Extrapolation of the modulation boundaries upward for larger forcing amplitudes in Figure 11 would indicate that these modulated waveforms could occur over a frequency range on the order of tenths of Hz for ship roll amplitudes of only 2°.

4.2 *The Chaotic Nature of the Pendulation Oscillations*

The stability (in a dynamic sense) of an oscillation to a perturbation is a useful piece of information. Stable orbits are defined as such by the fact that perturbations to them tend to “die out” over time and return the system to its previous state. If the perturbations tend to diverge such that different perturbations can lead to different system outcomes, the orbit is termed unstable. The tendency towards perturbation divergence is one of the most prominent features of a *chaotic* oscillation: the dynamics of a system in a chaotic regime

¹¹ In the experiment as well as in numerical simulation, the excitation was monotonically sinusoidal. The experimental forcing was conducted with a Stewart platform, which is a shaker table capable of being excited in all six axes of motion; Stewart platforms are used often as ship motion simulators.

¹² Appendix C contains a presentation of the mathematical modeling of the spherical pendulum and a review of the bifurcation analysis that leads to various types of motion.

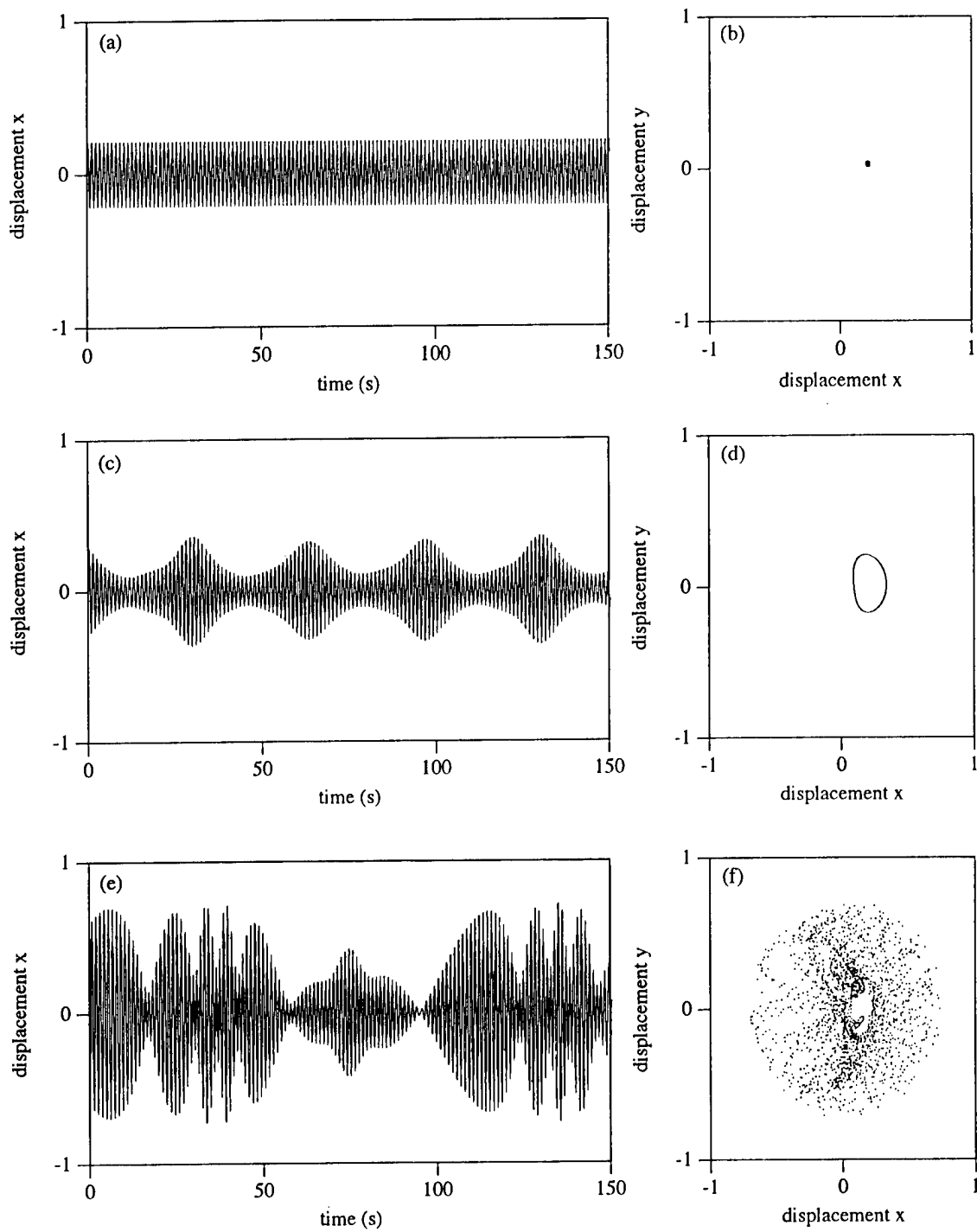


Figure 10. The appearance of amplitude modulations in the pendulum as the driving frequency approaches resonance from above (top plot to bottom plot). Stroboscopically-sampled versions (Poincaré sections) are also shown.

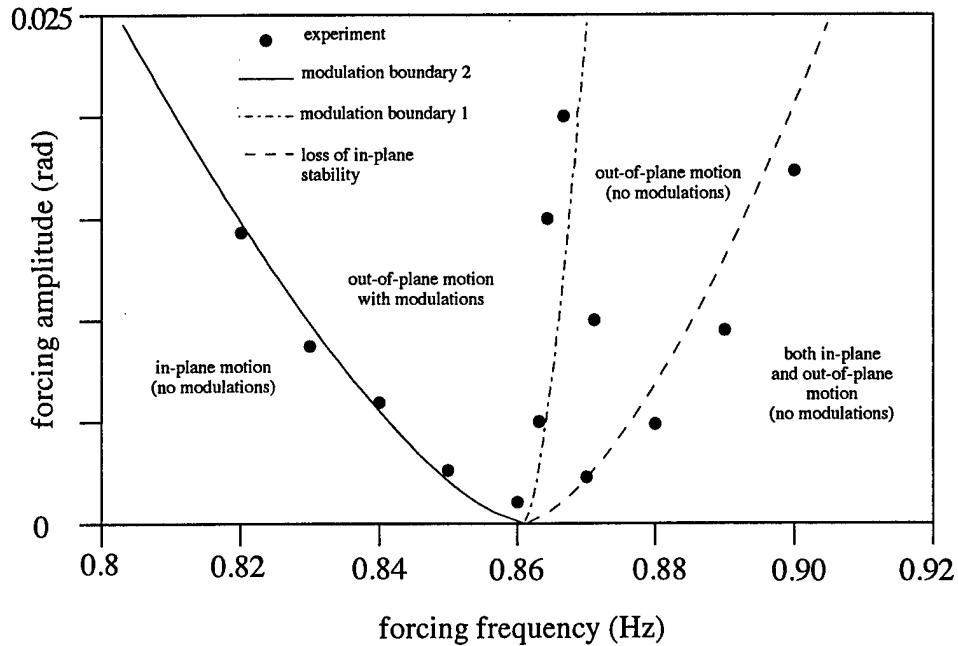


Figure 11. A global view of different dynamical regimes of the spherical pendulum; resonance is at 0.861 Hz.

are such that the phase space which completely describes the dynamics is expanding, at least locally. Of course, with any real system containing damping, the overall global effect upon phase space is one of net contraction, but locally, regions of expansion (and hence, instability) can exist.

These observations are summarized in Figure 12. In the top figure, two different (small) perturbations were applied to a pendulum oscillation in a region where the system is known to be non-chaotic. The two perturbations (red and blue traces) converge relatively rapidly upon the original oscillation. Conversely, the bottom part of the figure shows two perturbations being applied to the pendulum system when it is in a known chaotic region, *i.e.*, inside the modulation band. The perturbations stay together for a short while, but eventually they diverge under local expansion in the phase space. The multiplicative ergodic theorem [17] states that the nature of this convergence or divergence is contained in the system's Lyapunov exponents, which essentially measure a "rate" at which a family of perturbations tend to diverge or converge. Thus, a positive-valued exponent indicates divergence (instability) and a negative exponent indicates convergence (stability). The number of Lyapunov

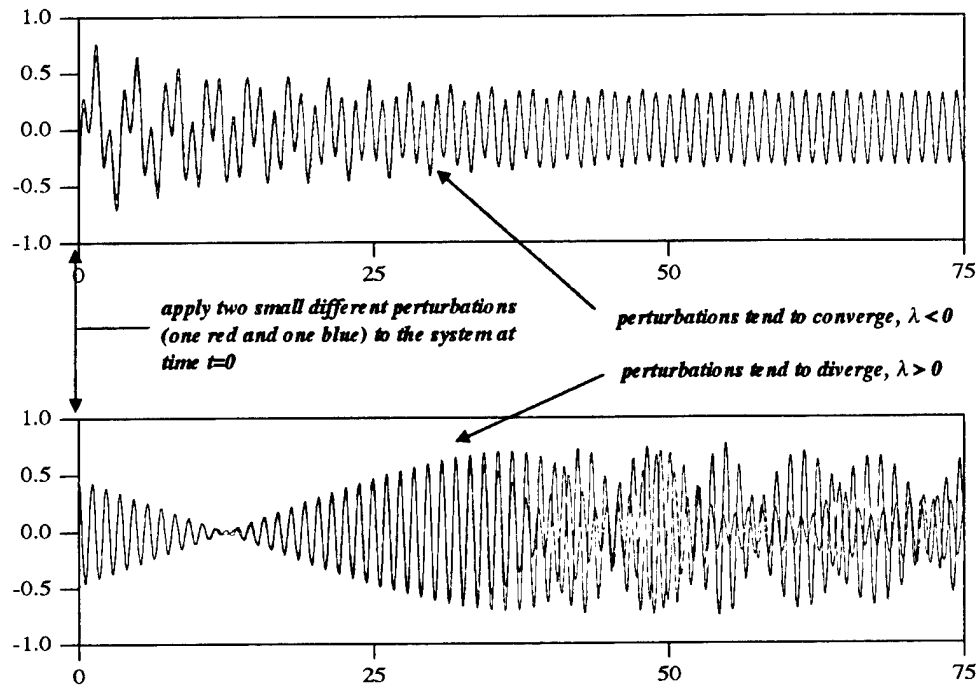


Figure 12. Lyapunov exponents give one measure of the stability of an oscillation to small perturbations.

exponents of a system is the same as the number of dynamical degrees of freedom that are needed to reconstruct fully the dynamics of the system¹³; though a system may have several Lyapunov exponents, if only one of them is positive, then the orbit is chaotic. As mentioned previously, determination of the chaotic nature of a system can dictate advanced control strategies [2].

Computation of Lyapunov exponents from a data set is a difficult task, primarily due to the inherent ill-conditioned nature of calculating the eigenvalues of the Oseledec matrix and from estimating Jacobian derivatives of the orbit [17]. Although recursive QR decomposition¹⁴ techniques and the “nearest neighbors” algorithms [18] have helped ease these difficulties, the calculation methods generally assume that the data that is *not* behaving simultaneously at separable time scales, such as with the crane load motion. Since the chaotic behavior of interest is only occurring at the slow time scale, it is necessary to

¹³ That is, to describe completely the phase space of the system at any given time.

¹⁴ This technique relies on the fact that any real matrix can be composed of the product of an orthogonal matrix and an upper triangular matrix.

isolate that behavior while retaining the important dynamical features. A phase-sensitive detection scheme, depicted in Figure 13, is used to do this. In this technique, the modulated output is multiplied by a reference signal oscillating at (typically) the dominant fast-time frequency ("carrier"), gain adjusted, and sharply low-pass filtered at a corner frequency between the highest modulation frequency that is desired to be seen and the carrier; when the separation of time scales is quite large, as in the system at hand, less care is needed in choosing the specific corner frequency of filtering so that relevant dynamics are retained. The gain adjustment is not critical, either; the filter output is attenuated by one-half the amplitude of the reference signal such that if the reference signal is an exact sinusoid, the appropriate amplitude of the original modulated signal will be exactly recovered.

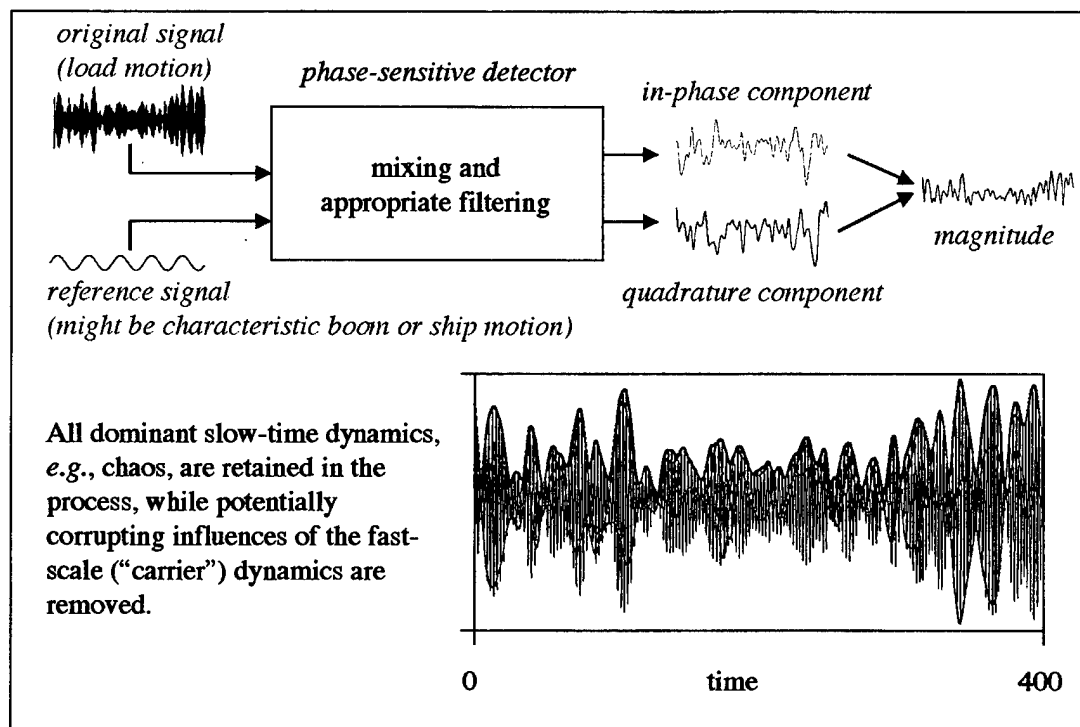


Figure 13. A phase sensitive detection technique isolates the slow-time behavior.

In a similar fashion, the same modulated output that was multiplied by the carrier reference is multiplied by a phase-shifted (usually $\pi/2$) carrier reference and likewise signal processed. The two resulting outputs are the in-phase and quadrature components of the demodulated signal, representing the phase-dependent modulations of the original signal¹⁵.

¹⁵ The terms "in-phase" and "quadrature" strictly apply only if the phases of the reference and the modulated signal are the same.

These outputs are directly analogous to the $f_i(\tau)$ of the slow-time mathematical model described in Appendix C (Equations 12). A more detailed description of this method and its relation to Poincaré sectioning can be found in [19].

4.3 Application to Model Test Crane Load Oscillations

Lyapunov exponents were computed for data from selected runs in the model test. The phase-sensitive detection technique was applied, and the nearest neighbors and QR decomposition algorithms were used to calculate the exponents from the subsequent slow-time data. Figure 14 compares the result between two different runs (both at sea state 3+swell but with different crane configurations). The red curve throughout is a pendulating load motion, and the blue curve throughout is non-pendulating. The top graph compares the power spectra of the corresponding full time series, which themselves are inset at the top right of the graph. The bottom inset shows the resulting slow-time series after processing through the phase-sensitive detection scheme described above. Once the fast-time dynamics have been removed, a complex motion remains in the pendulating case, while the an almost flat line remains in the non-pendulating case. The power spectrum of the pendulating case also shows its broader frequency content around the resonant peak, indicative of chaos. Calculations of global dimension for both cases resulted in a 3-D result¹⁶, shown at the bottom left of the figure; global dynamical dimension is determined when the percent of false nearest neighbors approaches zero. As mentioned, for every dimension a Lyapunov exponent can be calculated, and these results are shown at the bottom right of the figure. For the non-pendulating case, all three exponents are negative, while for the pendulating case, one exponent is positive. This implies that there is local instability to perturbation in the time series, and the time series is likely chaotic. One exponent in each case seems to be very close to zero, and this is due to the fact that perturbations made in the direction that the time series are already headed lead to a case of neutral stability (a zero exponent) [17]. These indications of chaos seemed to occur mostly in 2-D pendulation events; the 1-D pendulations events did not appear to be chaotic, although the motions were still quite large. It should be reiterated at this point that the preceding discussion has focused on key *nonlinear* aspects of load pendulation, and linear aspects will be addressed in a future

¹⁶ Another interpretation of this is that the full phase space can be described by three coordinates, and the attractor itself is unfolded in three dimensions.

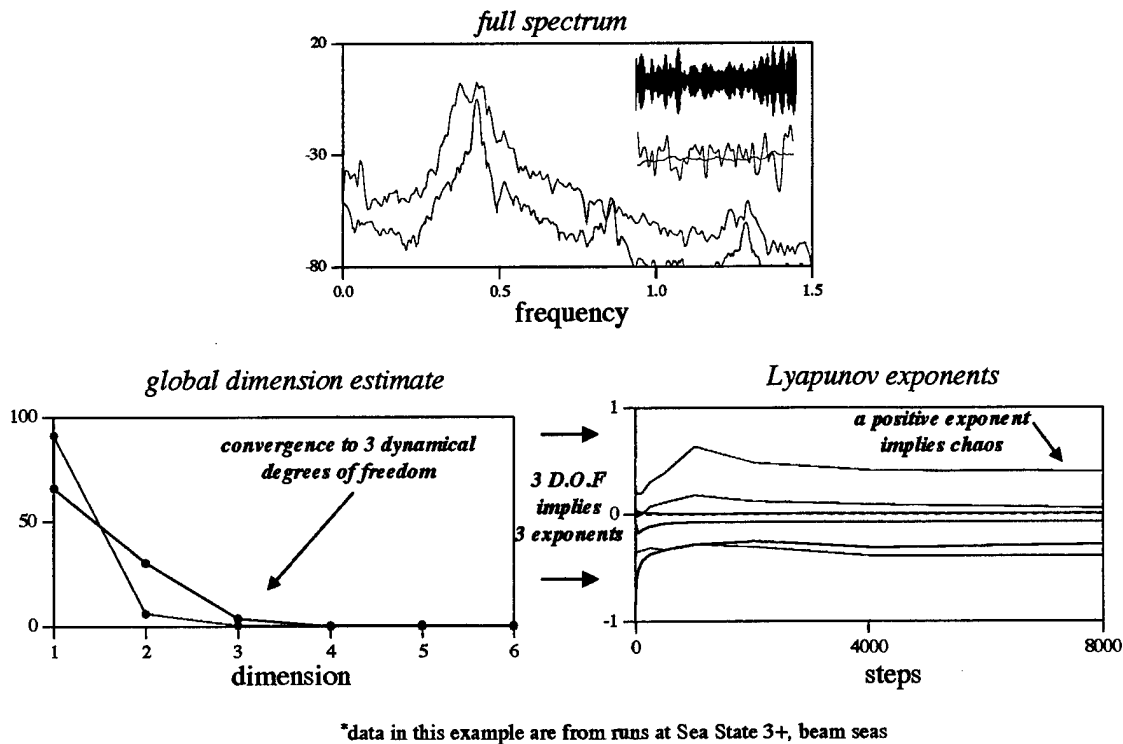


Figure 14. Comparison of the Lyapunov exponents calculated from a non-pendulating load oscillation and a pendulating load oscillation.

report.

5. T-ACS/Lighter Impact Events

The mooring configuration during the test allowed for periodic collisions between the various ships¹⁷. These impacts were initially detected by observing sharp peaks in the sway acceleration time history of the lighter (channels 45 and 46). In order to confirm spikes due to impact, the relative displacement between T-ACS and lighter in the sway direction (channel 29) was also monitored for sharp minima near zero¹⁸. Figure 15 shows an example (sea state 4+swell, beam seas); the sway acceleration trace is blue and the relative displacement trace is red. A number of instances are noted where a spike in the acceleration

¹⁷ Buoys were placed along both sides of the long axis of the T-ACS to prevent structural damage.

¹⁸ While a relative displacement reading of zero clearly implies contact between the ships, tolerances greater than zero had to be established because the lighter train does not always behave as a rigid body in sway, i.e., impact between ships could occur at one end but not near the center where the measurement was being taken.

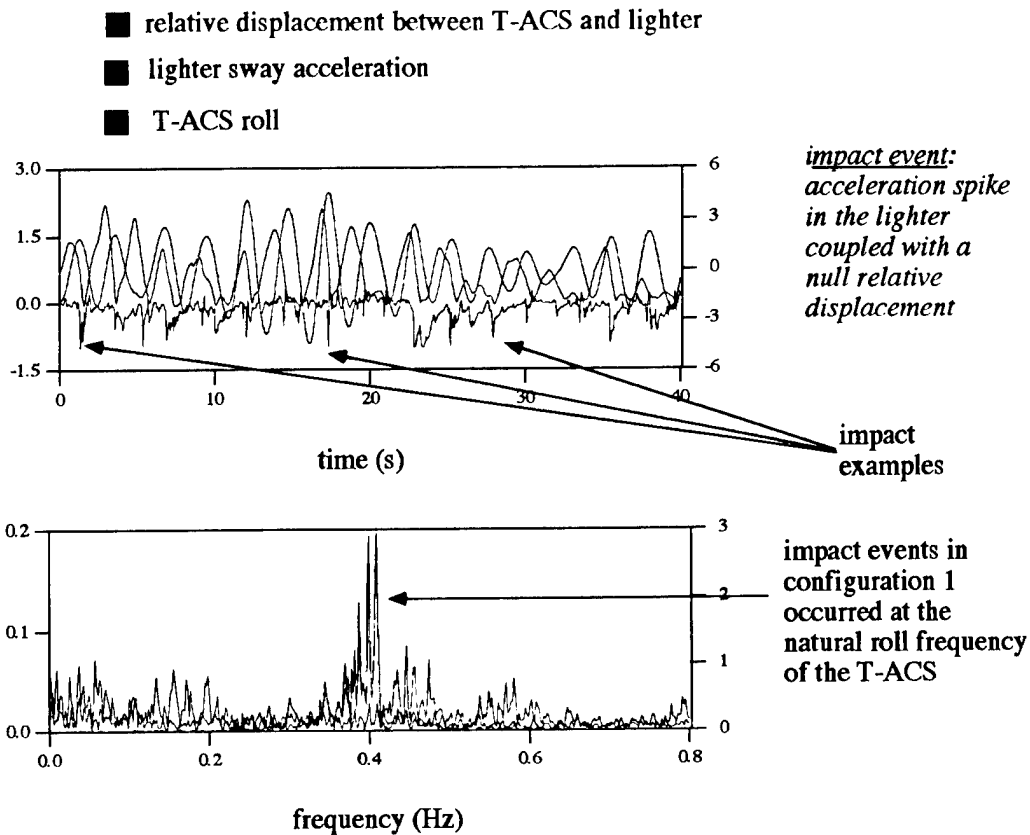


Figure 15. Lighter impacts with the T-ACS ship during the runs were significant; sway accelerometers detected spikes due to the impact forces, and these coupled with zero relative displacement readings between the craft.

trace corresponds to a near-zero minimum of the relative displacement trace. The T-ACS roll time history (green) is included for comparison, especially when their corresponding power spectra are compared in the plot below the time series. The spectra for the relative displacement and the T-ACS roll appear almost identical, implying that the impact events are occurring commensurate with the T-ACS roll. This result was noted for many runs where the ships were in a beam seas condition, and the lighter was leeward to the incoming wave group; head seas resulted in significantly fewer impacts, but generally the same frequency relationship. The blocking of the incoming waves by the container and T-ACS ships resulted in a local sea state around the lighters dominated by radiated waves off of the T-ACS hull. In this way, the T-ACS ship entrained the lighter array into its natural roll cycle. In ship configuration 2, where the container ship was removed and the lighters were no longer on the leeward side of the waves, this mode entrainment was no longer as

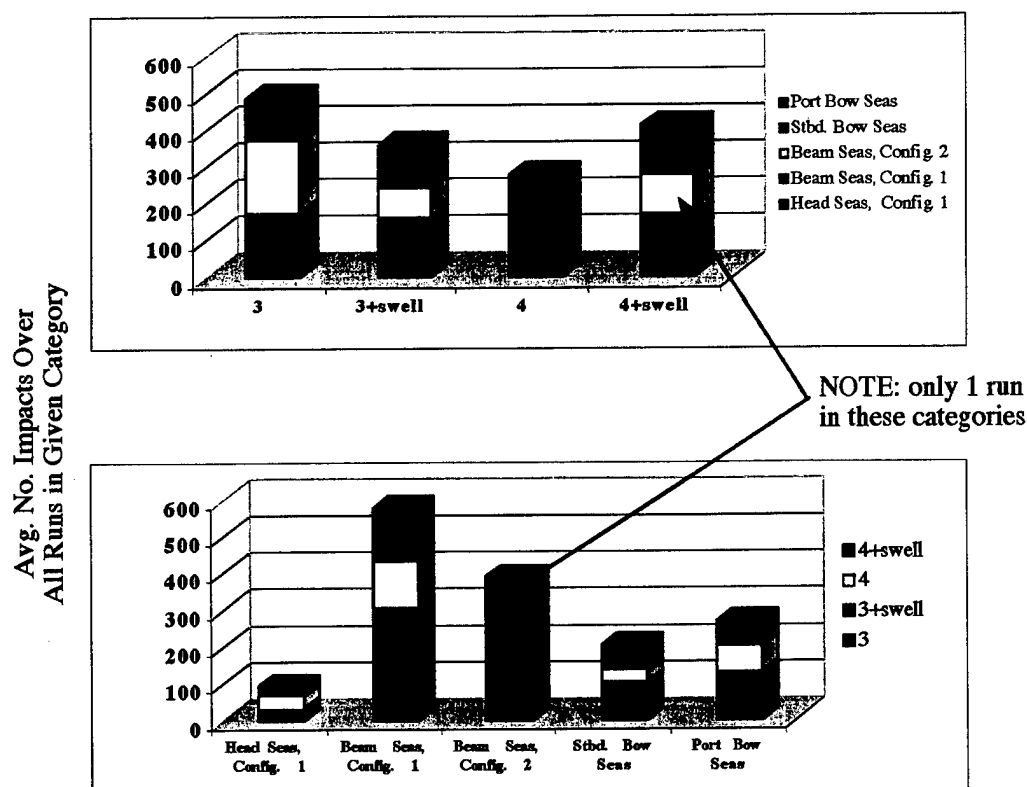


Figure 16. A categorization of impact events by sea state and ship heading and configuration

dominant a characteristic, and further study is warranted. In this latter case, the lighter senses the full effect of the sea state¹⁹, and it was noted that the impact events had broader frequency characteristics.

A summary of impact results is shown at the bottom of Figure 16, first grouped by sea state and then by ship configuration and heading. The values represent the average number of impacts noted over all runs that encompassed the given category. The most impacts occurred during beam seas, with somewhat fewer during bow seas, and significantly fewer during head seas. Configuration 1 beam sea conditions seemed to produce more impacts on average than configuration 2, and this is likely due to the frequency entrainment discussed previously. Of slightly puzzling consequence is the result that the higher sea states, such as 4 and 4+swell, did not, on average, produce larger numbers of impacts (for all ship and heading configurations) than did the lower sea states, such as 3 and 3+swell. While it could be hypothesized that the higher sea states should produce more impact events due to

¹⁹ Although, it is acknowledged that radiated waves off of the T-ACS still exist and contribute to the local sea state.

larger ship responses, it is apparent that heading and configuration are far more dominant variables than sea state.

6. Summary and Conclusions

This report has presented certain results regarding crane load pendulation dynamics and lighter barge/T-ACS impact events from a 1997 1:24 scale JLOTS model simulation in the David Taylor Model Basin at NSWC-Carderock. A description of the fiber optic accelerometer system designed to detect the lighter barge motions was also presented. The key results are summarized as follows:

- The crane load *pendulates* under certain sea states and ship headings; typically beam seas produce the most pendulation.
- Pendulation can be broadly classified as 1-D (large scale oscillations in one direction only) or 2-D (large scale oscillations in both directions).
- Pendulation is driven by the resonance condition of the load swing; when the RBTS is not used to maintain small resonance lengths, or when the tag lines are not pulled taught to implement the RBTS fully, pendulation is exacerbated in all sea states and ship headings.
- The crane load motion has been shown to be a two-timing system, like a spherical pendulum, with the fast-time oscillations commensurate with excitation (*i.e.*, ship roll) and the slow-time modulations of that motion due to inherent dynamical nonlinearity.
- The slow-time modulations can be isolated with a phase-sensitive detection scheme and have been shown to be chaotic with the appearance of a positive Lyapunov exponent; the chaotic cases of load motion seem to correspond mostly with 2-D pendulation.
- Lighter barge impacts with the T-ACS ship are significant (as frequent as 0.4-0.5 Hz), with the occurrence commensurate with T-ACS roll in ship configuration 1 due to frequency entrainment; ship configuration 2 does not support this conclusion.

The proper use of the RBTS is an important step (in current practice) in reducing pendulation. After the test, the model crane was removed from the the T-ACS ship and placed upon the Stewart platform for controlled testing. A short study on the use of RBTS in controlling resonance will be the subject of a future report. Further study is also warranted on impact event correlations, particularly in ship configuration 2.

7. Acknowledgments

The authors gratefully wish to acknowledge Greg Nau, Bruce Danver, Al Tveten, Dan Hayden, and Rich Bishop, all of whom contributed significantly either to various aspects of the model test itself or to the subsequent data analysis. We also gratefully wish to acknowledge Frank Leban for financial sponsorship and program oversight.

References

- [1] Theodore G. Vaughters. Joint logistics over the shore operations. *Naval Engineers Journal*, May:256–263, 1994.
- [2] E. Ott, C. Grebogi, and J. Yorke. Controlling chaos. *Physical Review Letters*, 64:1196, 1990.
- [3] S. Vohra, B. Danver, A. Tveten, and A. Dandridge. High performance fibre optic accelerometers. *Electron. Lett.*, 33:155–157, 1997.
- [4] A. Dandridge, A. B. Tveten, and T. G. Giallorenzi. Homodyne demodulation scheme for fiber optic sensors using phase generated carrier. *IEEE J. Quant. Electronics*, QE-18:1647–1653, 1982.
- [5] M. D. Todd, G. M. Nau, B. A. Danver, A. B. Tveten, and S. T. Vohra. A low-frequency fiber optic accelerometer array for mechanical motion detection. In *Proc. 12th Int. Conf. Optical Fiber Sensors*, pages 75–78, Williamsburg, VA, 1996.
- [6] S. W. Shaw and P. J. Holmes. A periodically forced piecewise linear oscillator. *Journal of Sound and Vibration*, 90:129–155, 1983.
- [7] S. R. Bishop, L. M. Leung, and L. N. Virgin. Predicting incipient jumps to resonance of compliant marine structures in an evolving sea-state. *ASME Journal of Offshore Mechanics and Arctic Engineering*, 109:223–228, 1987.
- [8] P. V. Bayly and L. N. Virgin. Chaotic rattling of a piecewise nonlinear oscillator. ASME Winter Annual Meeting, Atlanta, GA, December 1991.
- [9] M. D. Todd and L. N. Virgin. An experimental impact oscillator. *Chaos, Solitons, and Fractals*, 8(4):699–714, 1997.
- [10] Steven H. Strogatz. *Nonlinear Dynamics and Chaos*. Addison-Wesley, New York, 1994.
- [11] J. W. Miles. Resonant motion of a spherical pendulum. *Physica D*, 11:309–323, 1984.
- [12] D. J. Tritton. Ordered and chaotic motion of a forced spherical pendulum. *European Journal of Physics*, 7:162–169, 1986.
- [13] P. J. Bryant. Breakdown to chaotic motion of a forced, damped, spherical pendulum. *Physica D*, 64:324–339, 1993.
- [14] S. Tousi and A. K. Bajaj. Period-doubling bifurcations and modulated motions in forced mechanical systems. *Journal of Applied Mechanics*, 52:446–452, 1985.
- [15] M. D. Todd and S. T. Vohra. Transient dynamics of a lightly-damped, roll-forced pendulum. *Dynamics and Stability of Systems*, 13:95–115, 1998.
- [16] M. D. Todd and S. T. Vohra. Measurement and analysis of complex modulated motions in a weakly nonlinear system. *Physica D*, 1998. to appear.
- [17] H. D. I. Abarbanel. *Analysis of Observed Chaotic Data*. Springer, New York, 1996.

- [18] H. Abarbanel, R. Brown, and M. B. Kennel. Lyapunov exponents in chaotic systems: their importance and evaluation using observed data. *International Journal of Modern Physics B*, 5(9):1347–1375, 1991.
- [19] M. D. Todd and S. T. Vohra. An alternative to poincare sectioning in a weakly nonlinear system. *International Journal of Bifurcations and Chaos*, 1998. in review.
- [20] A. Leissa. *Vibration of Plates*. Acoustical Society of America, 1993.
- [21] Daniel D. Kana and Douglas J. Fox. Distinguishing the transition to chaos in a spherical pendulum. *Chaos*, 5:298–310, 1995.

A. Appendix: Channel Summary for 1:24 Scale Model Test

Channel descriptions for the first 32 channels can be found in Table 1. The fiber optic accelerometer channels (channels 33-46) were used to measure the lighter and crane motions, and their placement is shown in Figure 17.

Channel No.	Description	Units	Channel No.	Description	Units
01	Wave Height Bow	inches	17	Cntr CG XAcc	g
02	Sonix Sonic	inches	18	T-ACS/Cntr Rel X	in
03	T-ACS Roll	deg	19	T-ACS/Cntr Rel Y	in
04	T-ACS Pitch	deg	20	T-ACS/Cntr Rel Z	in
05	T-ACS Roll Rate	deg/s	21	Lhtr Roll	deg
06	T-ACS Pitch Rate	deg/s	22	Lhtr Pitch	deg
07	T-ACS Yaw Rate	deg/s	23	Lhtr Roll Rate	deg/s
08	T-ACS CG ZAcc	g	24	Lhtr Pitch Rate	deg/s
09	T-ACS CG YAcc	g	25	Lhtr CG XAcc	g
10	T-ACS CG XAcc	g	26	Lhtr CG YAcc	g
11	T-ACS CT ZAcc	g	27	Lhtr CG ZAcc	g
12	T-ACS CT YAcc	g	28	T-ACS/Lhtr Rel X	in
13	Cntr Roll	deg	29	T-ACS/Lhtr Rel Y	in
14	Cntr Pitch	deg	30	T-ACS/Lhtr Rel Z	in
15	Cntr CG ZAcc	g	31	Load Motion \perp Boom	in
16	Cntr CG YAcc	g	32	Load Motion \parallel Boom	in

Table 2. Descriptions for the non fiber-optic channels.

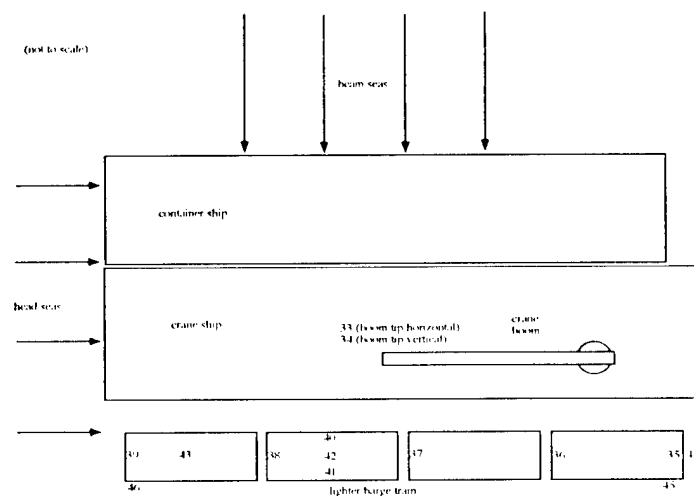


Figure 17. Placement of fiber optic accelerometers upon the lighter barge train and crane structure (channels 33-46).

B. Appendix: Flexural Disc Dynamics Theory

The free flexural (transverse) displacement $w(r, \theta)$ of a center-supported circular disc, under assumptions of classical thin-plate theory [20], obeys the partial differential equation (in polar coordinates)

$$\nabla^4 w + (\rho/D) w_{tt} = 0, \quad (2)$$

where the flexural rigidity $D = Eh^3/12/(1 - \nu^2)$, E is Young's modulus, h is the disc thickness, ν is Poisson's ratio, ρ is the density, and ∇^4 is the biharmonic operator. Center-supported boundary conditions imply no displacement or slope at the center of the disc, and no moments or shear forces at the free edge. Under further assumption that the disc bends primarily in its first symmetric mode (a "flap" mode) where there is no dependence upon θ , a separation of variables approach leads to the free-vibration, first-mode solution

$$w(r) = I_0(1.942r/R) - J_0(1.942r/R) + 2.496K_0(1.942r/R) + 3.921Y_0(1.942r/R), \quad (3)$$

where R is the radius of the disc, and J_0, Y_0, K_0 , and I_0 are Bessel functions of the first kind. This first-mode solution is shown in Figure 18.

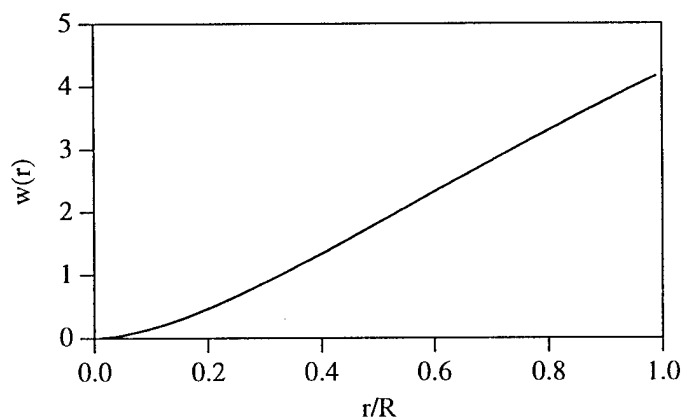


Figure 18. The first mode shape for a center-clamped circular disc.

To model the full forced disc-and-ring weight combination, we let $W(r, t) = q(t)w(r) + f \sin \omega t$, where $q(t)$ is the time-dependent modal coordinate²⁰, and $f \sin \omega t$ represents the added displacement (and hence, acceleration) due to the system being forced at the frequency ω . Taking a Lagrangian approach, the kinetic and elastic (potential) energy expres-

²⁰ As per the previous free vibration discussion, we choose $w(r)$ to be the center-clamped mode shape without a ring weight, i.e., equation (3).

sions can be written, respectively, as

$$\begin{aligned} T &= \pi h \rho \int_0^R (W_t)^2 r dr + (1/2) M (w(R))^2 \\ U &= D \pi \int_0^R (W_{rr} + (1/r) W_r)^2 - 2(1 - \nu) W_{rr} (1/r) W_r r dr, \end{aligned} \quad (4)$$

where the ring weight (of mass M) is assumed to be concentrated at the boundary ($r = R$). Computation of these integrals results in a linear equation of motion for $q(t)$ which can be solved to get a frequency response. The resonant frequency f_{res} (in Hz) is given by

$$f_{res} = \frac{3.668}{2\pi} \sqrt{\frac{D}{R^2 (\rho h R^2 + 1.366 M)}}, \quad (5)$$

where it is apparent that the addition of concentrated mass M at the boundary causes a resonance reduction. Typically, the optical fiber that is bound to the disc is wound circumferentially (spirally) such that it senses tangential strain, $\epsilon_\theta = \frac{h}{2r} (\frac{\partial W}{\partial r})$. The effective strain in the interferometer (assuming all strain on the disc surface is transferred to the fiber) can be thought of as the change in fiber length, ΔL , divided by the original fiber length L ; in terms of disc strain, the strain sensed by the interferometer is

$$\frac{\Delta L}{L} = \frac{\int_{r_1}^{r_2} \epsilon_\theta (2\pi/d_{fib}) r dr}{L}, \quad (6)$$

where d_{fib} is the outer diameter of the fiber itself, and r_1 and r_2 are the inner and outer radii of the wound fiber disc (see Figure 19). The change ΔL is then proportional to the phase shift $\Delta\phi$, which is detected by the interferometer and subsequent demodulation.

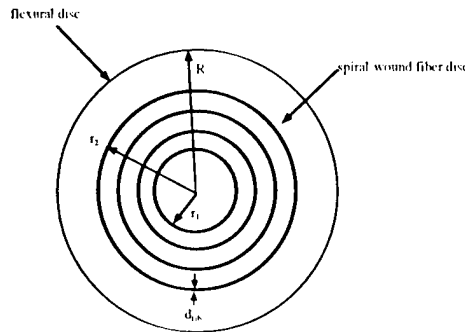


Figure 19. A flexural disc with a coil of optical fiber wound upon it.

C. Appendix: Mathematical Modeling of the Spherical Pendulum

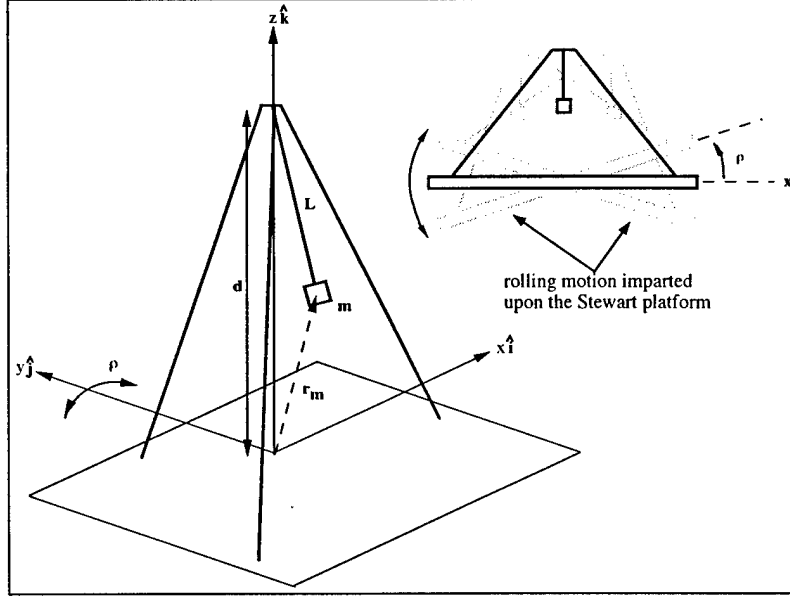


Figure 20. Coordinates used in modeling the spherical pendulum on a roll-shaken Stewart platform.

In order to mathematically model the roll-forced spherical pendulum, we consider a bob of lumped mass m attached to a rigid arm of length L that is suspended in the way shown in Figure 20. The suspension structure rests on top of a rigid platform that is forced to rotate about the y -axis through the time-dependent angle $\rho = \rho(t)$. The general displacement vector $\hat{\mathbf{r}}_m$ from the origin to the mass m can be written as

$$\hat{\mathbf{r}}_m = (x + d \sin \rho) \hat{\mathbf{i}} + y \hat{\mathbf{j}} + \left(d \cos \rho - \sqrt{L^2 - x^2 - y^2} \right) \hat{\mathbf{k}}, \quad (7)$$

where d is the height of the suspension structure above the platform base. If x and y are rescaled by the length L such that $x \equiv (x/L)$ and $y \equiv (y/L)$, an application of Lagrange's method to Eq. (7) yields the following equations of motion:

$$\begin{aligned} \mathcal{L}(x, y) = & \bar{d} \ddot{\rho} \left(x \sqrt{1 - x^2 - y^2} \sin \rho - (1 - x^2) \cos \rho \right) \\ & + \bar{d} \dot{\rho}^2 \left((1 - x^2) \sin \rho + x \sqrt{1 - x^2 - y^2} \cos \rho \right) \end{aligned} \quad (8)$$

$$\begin{aligned} \mathcal{L}(y, x) = & \bar{d} \ddot{\rho} \left(y \sqrt{1 - x^2 - y^2} \sin \rho + xy \cos \rho \right) \\ & + \bar{d} \dot{\rho}^2 \left(-xy \sin \rho + y \sqrt{1 - x^2 - y^2} \cos \rho \right), \end{aligned} \quad (9)$$

where the operator \mathcal{L} is defined by

$$\mathcal{L}(\xi, \eta) \equiv \ddot{\xi} + 2\zeta\omega_n\dot{\xi} + \omega_n^2\xi\sqrt{1-\xi^2-\eta^2} + \xi\left(\frac{\dot{\xi}^2 + \dot{\eta}^2 - (\eta\dot{\xi} - \xi\dot{\eta})^2}{1-\xi^2-\eta^2}\right), \quad (10)$$

and $\bar{d} = d/L$, $\omega_n = \sqrt{g/L}$ is the linearized resonant frequency of the pendulum, $\rho(t) = \rho_0 \sin \omega t$ is the periodic roll input angle of amplitude ρ_0 and frequency $\omega/2\pi$, and ζ is a linear damping coefficient. For the system at hand, a length of $L=33.5$ cm was chosen, corresponding to a resonant frequency of about 0.861 Hz. The damping ratio was measured to be on the order of 0.001 using a logarithmic decrement method. This light damping, similar to values reported by Tritton [12] and Kana and Fox [21], tends to promote resonant nonlinear behavior and long transients, the latter of which is less convenient for experimental study but more realistic of the actual crane systems in use.

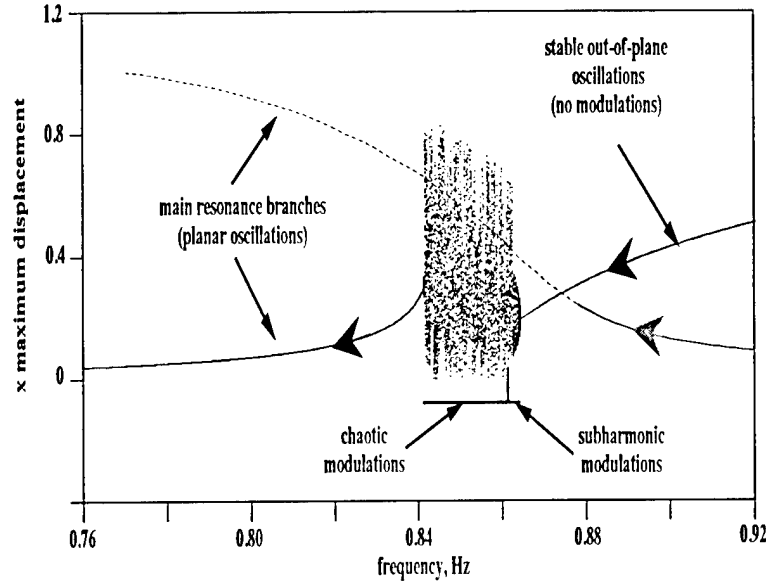


Figure 21. Bifurcation diagram of the spherical pendulum near resonance.

A global picture of the solutions admitted by Eqs. (8) and (9) is shown in the bifurcation diagram of Figure 21. In this diagram, the maximum displacement in x for fifty consecutive cycles is plotted as a function of the forcing frequency in a band $0.76 \leq \omega/2\pi \leq 0.92$ Hz. We shall discuss what occurs as the forcing frequency is decreased from right to left across the diagram: at $\omega/2\pi=0.92$, both an out-of-plane and an in-plane solution exist and are stable. The two *stable* solutions compete for trajectories under the inevitable dissipation due to damping. In this region, all motions for both solutions are monoperiodic and appear as

shown in Figure 10(a). As ω is decreased, the in-plane solution loses its stability (at about $\omega/2\pi=0.878$ in the case of Figure 21) such that for a small band ($0.8642 \leq \omega/2\pi \leq 0.878$), only out-of-plane harmonic behavior occurs. The unstable continuation of the in-plane solution is denoted by a dashed line. We note, as in [11] and [13], that this solution remains stable for a significantly larger frequency band when the pendulum is *plane-constrained*, but in the case of the spherical pendulum, the out-of-plane solution plays the more dominant role in the neighborhood of resonance.

With further decrease in forcing frequency, at approximately $\omega/2\pi=0.8642$, the monoperiodic out-of-plane solution also loses stability at a supercritical Hopf bifurcation [14] and gives rise to oscillations where the amplitudes are *modulated*, as the orbits move periodically with another frequency typically much smaller than the drive ω . The Poincaré section changes from a single point to a closed curve in the plane. The oscillations and Poincaré section in this Hopf-bifurcated region appear as the middle figures in Figure 10. The modulations themselves undergo a series of period-doublings (a flip bifurcation) [13] with continued reduction in drive frequency, until they become chaotic at the end of the cascade. The chaotically-modulated response exists for a finite frequency band, as was shown in the bottom figures of Figure 10, and then the in-plane solution is reacquired at about $\omega/2\pi=0.843$. The in-plane solution is again monoperiodic and linear-like in behavior.

Throughout this bifurcation sequence, recalling the time series of Figure 10, the drive frequency dominates the response, providing a strong “carrier” (*i.e.*, the fast-time behavior, as previously described) upon which the slow-time modulations are present. With the goal of isolating this slow-time behavior, a combination of multiple scales and slowly-varying amplitude/phase methods can be applied to Eqs. (8) and (9). The roll angle ρ_0 is chosen to be the perturbation (“small”) parameter ϵ , and, using a scheme similar to [11], the following orderings concerning the system variables and parameters are made:

$$\begin{aligned}
x(t, \tau; \epsilon) &= \epsilon^{1/3} (f_1(\tau) \sin \omega t + f_2(\tau) \cos \omega t) + O(\epsilon) \\
y(t, \tau; \epsilon) &= \epsilon^{1/3} (f_3(\tau) \sin \omega t + f_4(\tau) \cos \omega t) + O(\epsilon) \\
\tau &= \frac{1}{2} \epsilon^{2/3} \omega t \\
\omega^2 &= \omega_n^2 (1 + \gamma \epsilon^{2/3}) \\
\zeta &= \frac{1}{2} \kappa \epsilon^{2/3}.
\end{aligned} \tag{11}$$

This ordering allows for balance, to order ϵ , of all significant driving, damping, and non-

linearity near resonance. Substitution of Eqs. (11) into Eqs. (8) and (9) and neglect of all terms smaller than $O(\epsilon)$ yields the following slow-time system of equations:

$$\begin{aligned}
df_1/d\tau &= +\frac{1}{8}f_1^2f_2 + \frac{1}{8}f_2^3 - \frac{5}{8}f_2f_3^2 + \frac{3}{4}f_1f_3f_4 + \frac{1}{8}f_2f_4^2 - \kappa f_1 + \gamma f_2 \\
df_2/d\tau &= -\frac{1}{8}f_2^2f_1 - \frac{1}{8}f_1^3 + \frac{5}{8}f_1f_4^2 - \frac{3}{4}f_2f_3f_4 - \frac{1}{8}f_1f_3^2 - \kappa f_2 - \gamma f_1 - \bar{d} \\
df_3/d\tau &= +\frac{1}{8}f_3^2f_4 + \frac{1}{8}f_4^3 - \frac{5}{8}f_4f_1^2 + \frac{3}{4}f_1f_2f_3 + \frac{1}{8}f_4f_2^2 - \kappa f_3 + \gamma f_4 \\
df_4/d\tau &= -\frac{1}{8}f_4^2f_3 - \frac{1}{8}f_3^3 + \frac{5}{8}f_3f_2^2 - \frac{3}{4}f_1f_2f_4 - \frac{1}{8}f_3f_1^2 - \kappa f_4 - \gamma f_3
\end{aligned} \tag{12}$$

Eqs. (12) essentially can be interpreted as describing the motion of the amplitude “envelope” of the full response governed by Eqs. (8) and (9). This system of equations can then be analyzed to determine global dynamical properties, such as the modulation boundaries of Figure 11.

REPRODUCTION QUALITY NOTICE

This document is the best quality available. The copy furnished to DTIC contained pages that may have the following quality problems:

- **Pages smaller or larger than normal.**
- **Pages with background color or light colored printing.**
- **Pages with small type or poor printing; and or**
- **Pages with continuous tone material or color photographs.**

Due to various output media available these conditions may or may not cause poor legibility in the microfiche or hardcopy output you receive.



If this block is checked, the copy furnished to DTIC contained pages with color printing, that when reproduced in Black and White, may change detail of the original copy.